SI Appendix – Correlated topological flat bands in rhombohedral graphite

Hongyun Zhang,[1,*] Qian Li,[1,*] Michael G. Scheer,[2] Renqi Wang,[1] Chuyi Tuo,[3] Nianlong Zou,[1] Wanying Chen,[1] Jiaheng Li,[1] Xuanxi Cai,[1] Changhua Bao,[1] Ming-Rui Li,[3] Ke Deng,[1] Kenji Watanabe,[4] Takashi Taniguchi,[5] Mao Ye,[6] Peizhe Tang,[7,8] Yong Xu,[1,9] Pu Yu,[1,9] Jose Avila,[10] Pavel Dudin,[10] Jonathan D. Denlinger,[11] Hong Yao,[3] Biao Lian,[2] Wenhui Duan,[1,3,9] and Shuyun Zhou[1,9,†]

[1]*State Key Laboratory of Low-Dimensional Quantum Physics and Department of Physics, Tsinghua University, Beijing 100084, P. R. China*

[2]*Department of Physics, Princeton University, Princeton, New Jersey 08544, USA*

[3]*Institute for Advanced Study, Tsinghua University, Beijing 100084, P. R. China*

[4]*Research Center for Functional Materials, National Institute for Materials Science, 1-1 Namiki, Tsukuba 305-0044, Japan*

[5]*International Center for Materials Nanoarchitectonics, National Institute for Materials Science, 1-1 Namiki, Tsukuba 305-0044, Japan*

[6]*Shanghai Synchrotron Radiation Facility, Shanghai Advanced Research Institute, Chinese Academy of Sciences, Shanghai 201210, P. R. China*

[7]*School of Materials Science and Engineering, Beihang University, Beijing 100191, P. R. China*

[8]*Max Planck Institute for the Structure and Dynamics of Matter, Center for Free Electron Laser Science, Hamburg 22761, Germany*

[9]*Frontier Science Center for Quantum Information, Beijing 100084, P. R. China*

[10]*Synchrotron SOLEIL, L'Orme des Merisiers, Saint Aubin-BP 48, 91192 Gif sur Yvette Cedex, France*

[11]*Advanced Light Source, Lawrence Berkeley National Laboratory, Berkeley, California 94720, USA*

*These authors contributed equally to this work.
†Correspondence should be sent to syzhou@mail.tsinghua.edu.cn

Contents:

Supplementary Materials

I. CALCULATED ELECTRONIC STRUCTURE AND TOPOLOGICAL PROPERTIES OF RG USING THE SLONCZEWSKI-WEISS-MCCLURE MODEL.

Electronic structures of RG were calculated by utilizing the tight-binding Slonczewski-Weiss-McClure model [1–3]. Here only the p_z-orbitals of carbons are considered, and the hopping terms mainly include intralayer and interlayer nearest-neighbor couplings, denoted as t_0 and γ_0 respectively. Additionally, γ_1 accounts for interlayer coupling between the next-nearest layers, while γ_2 and γ_3 represent weaker interlayer hoppings between the nearest layers. To reveal the low-energy physics near E_F of finite N-layered RG, which is dominated by the surface states, we use an effective $\mathbf{k}\cdot\mathbf{p}$ model incorporating the Slonczewski-Weiss-McClure tight-binding parameters [4, 5]. The projection of this Hamiltonian onto the two-band form within the basis of surface sites [3, 4] can be expressed as:

$$\hat{H}_N^{\text{eff}} = \begin{pmatrix} \frac{p^2}{2m} & X(p) \\ X^\dagger(p) & \frac{p^2}{2m} \end{pmatrix} \tag{1}$$

and the low energy dispersion is expressed by:

$$\begin{aligned} X(p) = \sum_{\{n_1,n_2,n_3\}} & \frac{(n_1+n_2+n_3)!}{n_1!n_2!n_3!} \frac{1}{(-\gamma_0)^{n_1+n_2+n_3-1}} \\ & \times \left(v_0 p e^{i\eta\phi}\right)^{n_1} \left(v_2 p e^{-i\eta\phi}\right)^{n_2} \left(\frac{\gamma_1}{2}\right)^{n_3} \end{aligned} \tag{2}$$

where η is the valley index and $\mathbf{p} = p(\cos\phi, \sin\phi)$ is measured from K or K′, v_0 and v_2 are the Dirac velocity related to t_0 and γ_2. The summation is carried out under the constraint $n_1+2n_2+3n_3 = N$ and $n_i \geq 0$. Given that γ_1 and v_2 are much weaker, $X(p)$ can be simplified to $X(p) \approx (v_0 p e^{i\eta\phi})^N/(-\gamma_0)^{N-1}$. Figure S1 shows the calculated electronic structure for N = 4, 5, 8, 10 and 20, from which we see that the bandwidth of the flat band decreases with increasing layer number.

Calculations for bulk RG, taking into account the dominant coupling terms t_0 and γ_0, reveal the existence of degenerate nodal lines protected by $\mathcal{PT}$ symmetry. These nodal lines rotate around the inequivalent corners K and K′ along the k_z direction with opposite chiralities, and the projection of each nodal line onto the 2D plane forms a circle. Moreover, the $\mathcal{PT}$ symmetry quantizes the Zak phase to be either 0 or π, allowing for $\mathbb{Z}_2$ topological

classification through the Wilson loop $\phi(\mathbf{k}_{||}) = \sum_n \int \mathbf{A_{nk}} \cdot \mathbf{k}_\perp$ perpendicular to a 2D plane [6]. This expression involves a summation over the band index n, and the Berry connection of the nth band is denoted as $\mathbf{A}_{n\mathbf{k}} = i\langle u_{n\mathbf{k}}|\partial_{\mathbf{k}} u_{n\mathbf{k}}\rangle$ where $|u_{n\mathbf{k}}\rangle$ represents the periodic part of the electronic Bloch wavefunctions. The calculations of the Wilson loop demonstrate that the nodal lines are topological, signifying that the quantized Zak phase changes by π across the projection of the nodal lines. In the region enclosed by the topological nodal line projections, the Zak phase value is π, indicating the existence of two zero-energy flat band surface states according to the topological bulk-boundary correspondence. Outside this region, the Zak phase is 0 and does not give surface states.

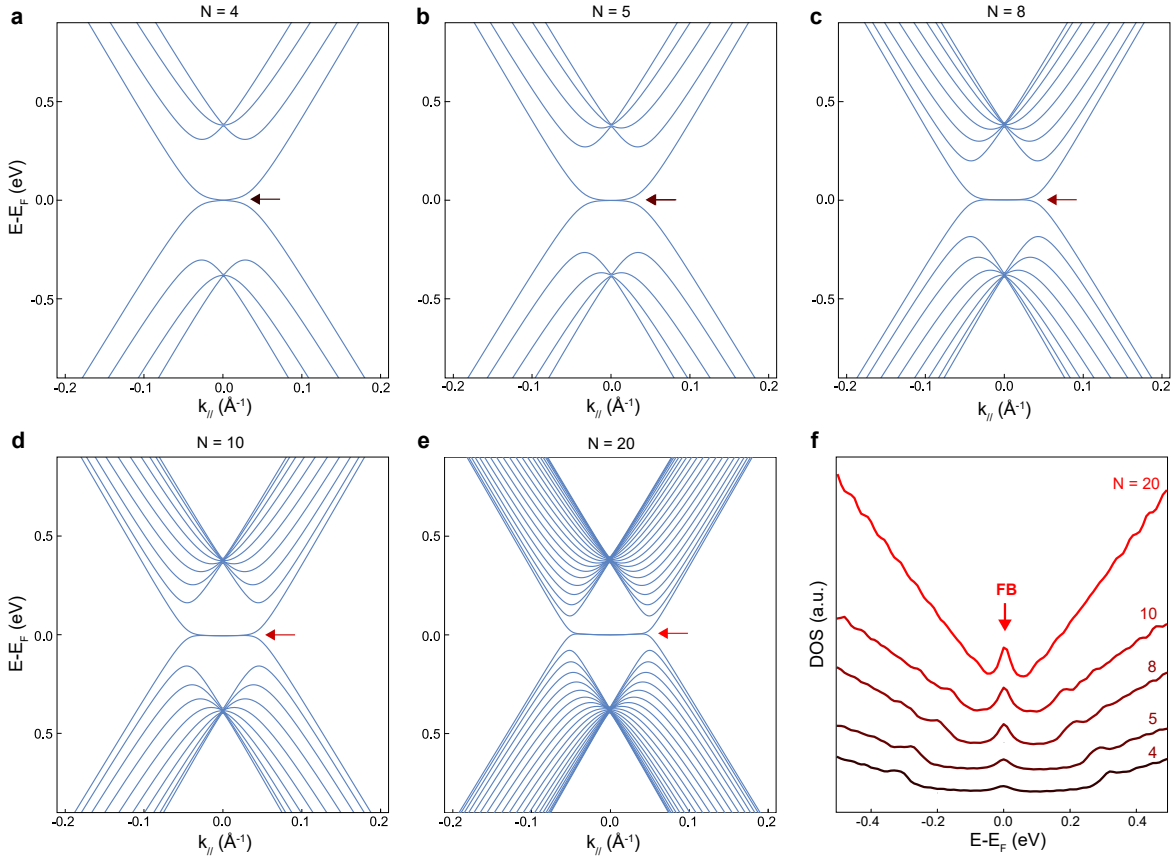

FIG. S1: **Calculated electronic structure for RG with varying number of layers. a-e**, Calculated electronic structure through the K point of RG with layer numbers $N = 4, 5, 8, 10$, and 20. The arrows with colors ranging from black to red indicate the TFBs which narrow as N increases. **f**, Comparison of the calculated density of states (DOS) for RG with $N = 4, 5, 8, 10$, and 20. The calculations were performed using the tight-binding Slonczewski-Weiss-McClure model.

II. SAMPLE PREPARATION AND CHARACTERIZATION.

The bulk RG samples were prepared using a clean dry transfer method. First, graphite flakes were exfoliated by Polydimethylsiloxane (PDMS), and the stacking of RG was identified by Raman spectroscopy measurements (see Fig. S2f). Second, the RG flakes were transferred onto substrates such as a gold-coated substrate (sample S1, sample S3 and sample S5), a p-type Si substrate (sample S2), or BN/Au/SiO_2//Si (sample S4) to ensure good electrical conductivity for ARPES measurements. Before ARPES measurements, the RG stacking was further confirmed by spatially-resolved Raman spectroscopy to verify that the stacking order did not change during the transfer process. Figure S2 shows an overview of five representative RG samples that have been measured. Although these samples were deposited on different substrates and with different thicknesses, they all show similar surface TFBs near E_F (indicated by red arrows in Fig. S2g-k).

Figure S3 shows more detailed characterizations of sample S5 by combining spatially-resolved Raman spectroscopy, ARPES and atomic force microscopy (AFM) measurements. Figure S3a shows an optical image of S5, and Raman spectra measured at a few representative positions are shown in Fig. S3b. According to previous reports [7], RG is characterized by a stronger $2D_L$ peak, and therefore the intensity ratio between $2D_L$ and $2D_R$ peaks, I_{2D_L}/I_{2D_R}, can be used to distinguish RG from Bernal graphite. Figure S3c shows the Raman intensity contrast map (I_{2D_L}/I_{2D_R}), where regions of RG and Bernal graphite are clearly distinguishable. Figure S3e shows a spatially resolved NanoARPES intensity map measured near E_F, where RG and Bernal stacking regions are also resolved. Representative NanoARPES dispersion images measured on RG (Fig. S3d) and Bernal graphite (Fig. S3f) further confirm their distinctive dispersions, where the TFBs in RG lead to a stronger intensity over the rectangular box near E_F. Figure S3g,h shows AFM measurements. The thickness of sample S5 is determined to be 10.4 nm, which corresponds to $N = 31$ layers. We would like to note that this thickness is enough to be considered as a bulk sample, and it shows overall similar experimental results with the other four thicker samples (Fig. S2). By combining optical images, Raman spectroscopy, NanoARPES, and AFM measurements, we are able to identify RG regions and obtain the intrinsic electronic structure from RG.

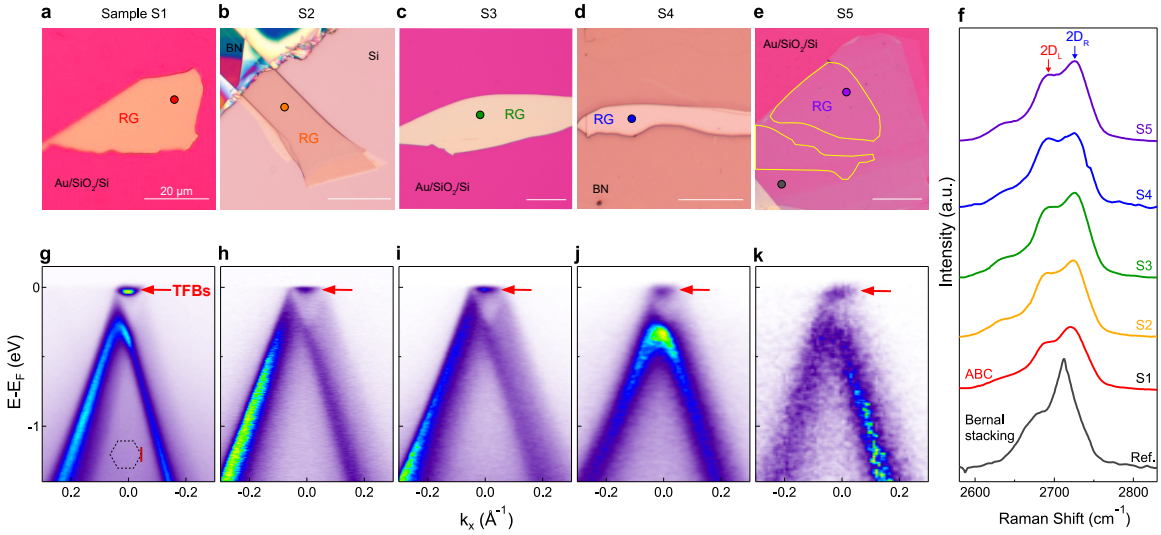

FIG. S2: **Surface TFBs observed on five representative RG samples. a-e**, Optical images of five representative RG samples. **f**, Raman spectra measured at colored spots from sample S1 to S5 to confirm the ABC stacking. The reference spectrum for Bernal (AB) stacking is measured on sample S5 (marked by gray dot). **g-k**, ARPES dispersion images measured along the red line indicated by the inset in **g**. Surface TFBs (indicated by red arrows) are observed in all samples.

III. ARPES MEASUREMENTS.

MicroARPES and NanoARPES measurements were performed at a vacuum better than 2×10^{-10} torr at beamline 4.0.3 of the Advanced Light Source at Lawrence Berkeley National Laboratory (LBNL), ANTARES of the Synchrotron SOLEIL in France, and BL03U of the Shanghai Synchrotron Radiation Facility (SSRF), with beam sizes of 30 μm, 500 − 700 nm, and 15 − 20 μm, respectively. Before ARPES measurements, the RG samples were annealed at 200°C in ultrahigh vacuum (UHV) until sharp dispersions were observed. The surface electron doping was achieved by *in situ* deposition of Rb through heating an SAES commercial dispenser.

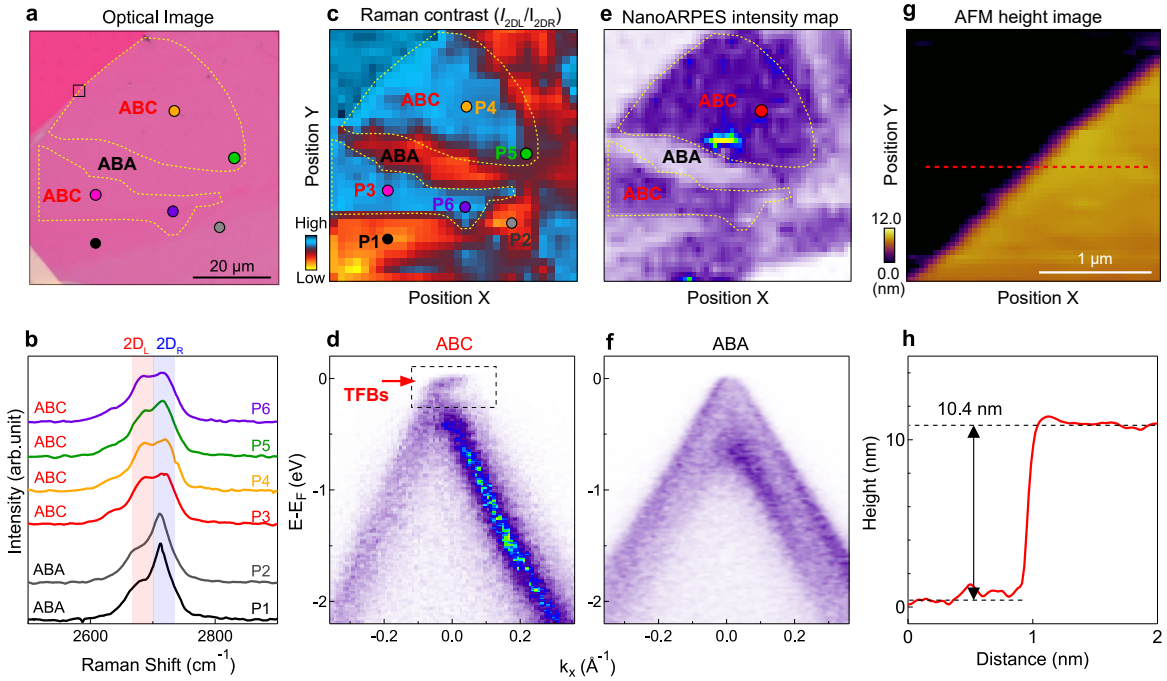

FIG. S3: **Characterization of RG stacking by Raman spectroscopy, AFM and NanoARPES on sample S5.** **a**, Optical image of RG sample S5 deposited on a $Au/SiO_2/Si$ substrate. **b**, Raman spectrum taken from positions P1 to P6 as labeled by colored spots in **c**. **c**, Raman intensity contrast by taking the intensity ratio of $2D_L/2D_R$ as indicated by color-shaded regions in **b**. The spatial map is taken with the same range as **a**, where higher intensity corresponds to RG and the substrate, and lower intensity corresponds to Bernal stacking region. **d**, Dispersion image measured on the RG region (red dot in **e**). **e**, NanoARPES spatial intensity map obtained by integrating over the black broken box in **d**. Higher intensity corresponds to RG regions with surface TFBs, while lower intensity corresponds to Bernal stacking regions and the substrate. **f**, Dispersion image measured on a Bernal graphite sample. **g, h**, AFM image and the height line profile to show the thickness of 10.4 nm which corresponds to RG with N = 31 layers.

IV. EXTRACTION OF THE BANDWIDTH AND MOMENTUM RANGE OF THE TFBS.

Figure S4 shows a comparison of ARPES spectrum with calculated dispersion. The ARPES data reveals the topological flat bands, plus bulk Dirac cone at one k_z value corresponding to the photon energy used. Here the photon energy is 70 eV, corresponding to $k_z = 2.28c^*$ (here $c^* = 2\pi/c$), and the experimental bulk Dirac cone is in good agreement with

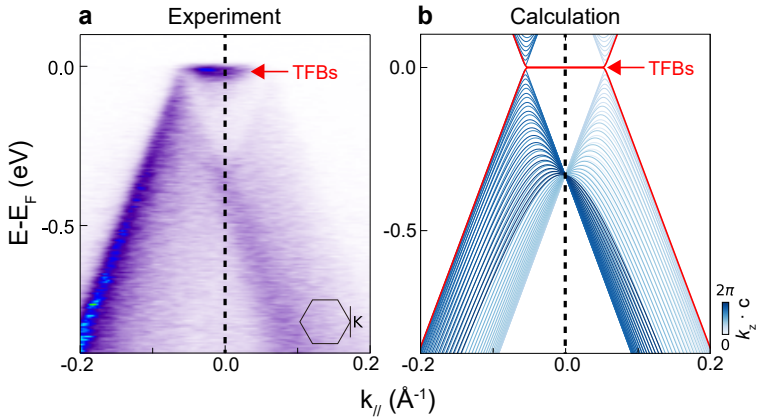

FIG. S4: **Comparison between ARPES data with calculated dispersion. a**, ARPES data taken under 70 eV with the measurement direction indicated by the inset. **b**, Calculated dispersion with the same direction as **a**. Different colors indicate bands from different k_z, and the red curves indicates the surface state band.

the calculation.

The momentum range of the TFBs is determined from the parallel cuts along k_x and k_y directions as shown in Fig. S5, from which a momentum range of $0.10 \pm 0.02\,\text{Å}^{-1}$ is determined. The bandwidth of the TFBs is extracted by performing the energy distribution curve (EDC) analysis. Figure S5i,j shows the EDC analysis, from which the bandwidth is extracted to be $32 \pm 7\,\text{meV}$.

V. COMPARISON OF DISPERSION IMAGES BETWEEN RHOMBOHEDRAL GRAPHITE AND BERNAL GRAPHITE.

Figure S6 shows a comparison of dispersion images measured on RG and Bernal graphite with photon energy from 35 eV to 80 eV (corresponding k_z changes from $1.61c^*$ to $2.43c^*$) by cutting through the K point. The RG shows a coexistence of a flat band and a Dirac node rotating from the right side of the flat band to the left side, while in contrast, Bernal graphite shows a spectral weight transfer between the outer and inner bands, and there is an evolution from electron pockets at 35 eV to hole pockets at 80 eV near E_F for the outer band, similar to previous results [9]. The above comparison shows that RG shows distinctive electronic structure from Bernal graphite, and that the topological flat bands and bulk helical Dirac nodal lines are intrinsic only to bulk RG.

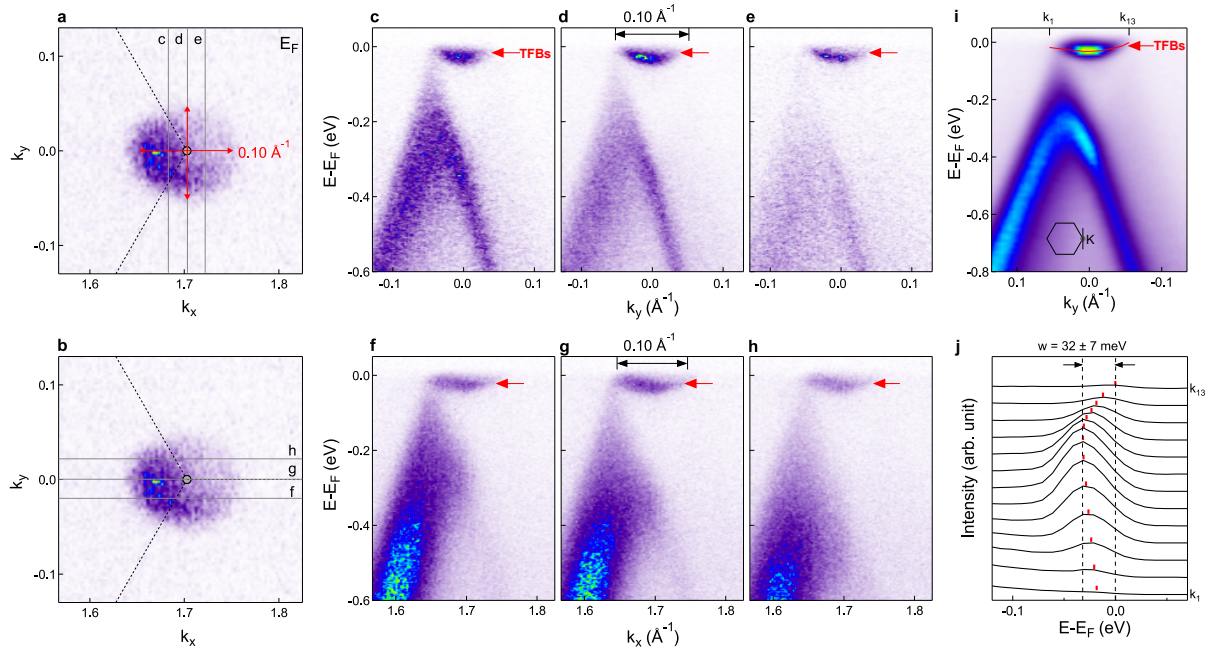

FIG. S5: **Extraction of the bandwidth and momentum range of the TFBs. a, b**, Fermi surface map measured at 60 eV photon energy on sample S1. The gray lines mark the momentum directions for data shown in **c-e** and **f-h** respectively. **c-e**, Dispersion images measured by cutting along the vertical directions (gray lines in **a**). **f-h**, Dispersion images measured by cutting along the horizontal directions (along the gray lines in **b**). The momentum range is $\Delta k = 0.10 \pm 0.02$ Å^{-1} along both horizontal and vertical directions. **i**, Dispersion image measured along the black line indicated by the inset. **j**, EDCs extracted from k_1 to k_{13} as indicated by red curve in **i**, from which the bandwidth of the TFBs is extracted to be 32 ± 7 meV.

VI. HELICAL DIRAC NODES WITH OPPOSITE CHIRALITIES AT K AND K′.

The Dirac node rotates around the K and K′ when changing k_z, with the period of the k_z Brillouin zone of rhombohedral graphite. Figure S7 shows the rotation of helical Dirac nodes, which rotates 90° when the k_z changes from 0 to $c^*/4$. The opposite helicities for the Helical DNLs near the K and K′ points are confirmed by Fig. S8,9. Figure S8 shows the helical Dirac nodal lines from ARPES measurements and calculation, which shows good agreement that the nodal lines rotate along opposite directions at K and K′ point. The Dirac node rotates 360° within one k_z Brillouin zone (Fig. S7a) [8]. To directly compare between the experiments and calculations, we show in Fig. S7b the calculated Dirac nodes at $k_z =$

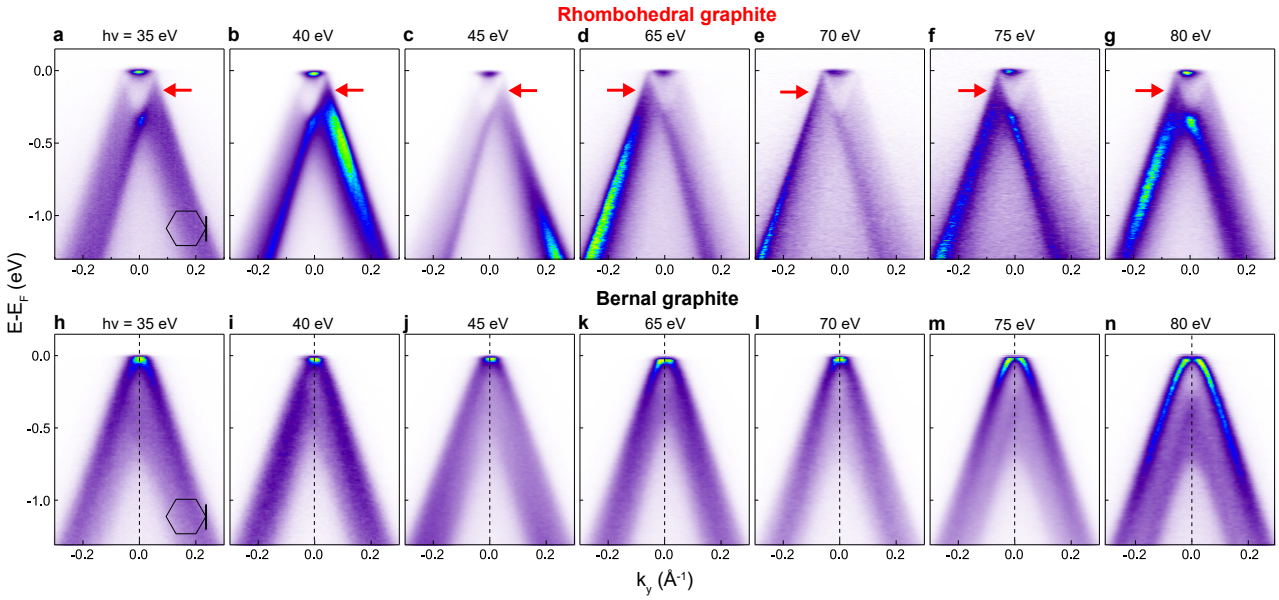

FIG. S6: **Comparison between the dispersion images of Rhombohedral and Bernal graphite measured at different photon energies (corresponding to different k_z values).** **a-g**, Dispersion images of Rhombohedral graphite measured under photon energy from 35 eV to 80 eV. The measurement direction is perpendicular to the Γ-K direction as indicated by the inset in **a**. **h-n**, Dispersion images of Bernal graphite corresponding the same photon energies and measurement direction as **a-g**. All dispersion images show mirror symmetry with respect to the black dotted lines.

0 and $k_z = c^*/4$ (indicated by red spots), which rotates along the projected surface state (gray curve). The energy contours measured at -100 meV using probe photon energies of 40, 50, and 70 eV are shown in Fig. S9b, from which we see that the nodal point rotates in opposite directions in the plane at the same k_z. The opposite chiralities are also confirmed in the dispersion images measured by cutting through the nodal points around the K and K′ points, reflecting the C_3 symmetry of RG.

VII. HARTREE-FOCK CALCULATIONS.

We now give a brief explanation of the projected Hartree-Fock calculations performed for Fig. 5 and Fig. S10. We consider a semi-infinite RG system with periodic boundary conditions in each layer. We label the layers $l = 0, 1, 2, \ldots$ where $l = 0$ is the top layer. We

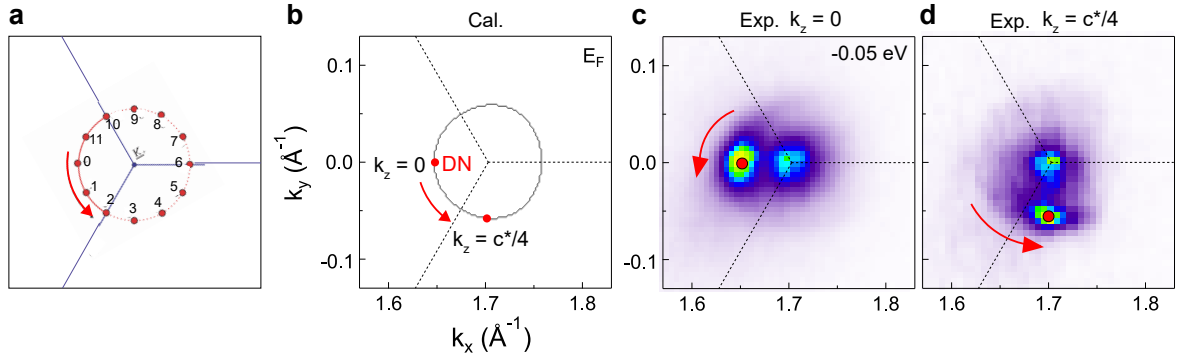

FIG. S7: **Comparison between the experimental and calculated helical Dirac node at $k_z = 0$ and $k_z = c^*/4$.** **a**, Rotation of the Dirac node with changing of k_z, adapted from (Phys. Rev. B 93, 075437 (2016) [8]). **b**, Calculated Dirac node (red points) at $k_z = 0$ and $k_z = c^*/4$. The gray circle indicates the projection of Dirac nodes from all k_z. **c,d**, Energy contours at -0.05 eV to show the rotation of Dirac node (indicated by pink dots) at $k_z = 0$ and $k_z = c^*/4$, respectively. Here **c** and **d** are measured under photon energy of 50 eV and 70 eV, corresponding to $k_z = 1.93c^*$ (close to $k_z = 0$ in the reduced Brillouin zone) and $k_z = 2.28c^*$ (close to $k_z = c^*/4$ in the reduced Brillouin zone), respectively. The spot at the center K point is the intensity tail of the bottom of TFB.

define the operator $c^\dagger_{\mathbf{p},s,\eta,l,\alpha}$ which creates an electron in valley $\eta \in \{+,-\}$ with momentum $\eta\mathbf{K} + \mathbf{p}$, spin $s \in \{\uparrow,\downarrow\}$, layer $l \geq 0$, and sublattice $\alpha \in \{A,B\}$. The non-interacting Hamiltonian is

$$H_0 = \sum_{\mathbf{p},s,\eta} \sum_{l',l=0}^{\infty} (f_{\mathbf{p},\eta}\delta_{l',l} + \gamma_0\delta_{l',l-1}) c^\dagger_{\mathbf{p},s,\eta,l',B} c_{\mathbf{p},s,\eta,l,A} + h.c. \tag{3}$$

where $f_{\mathbf{p},\eta} = \hbar v_F(\eta p_x + i p_y)$ is the Dirac cone dispersion and $\gamma_0 = 0.33\,\text{eV}$ is the out-of-plane hopping. Here, $v_F = \frac{at_0\sqrt{3}}{2\hbar}$ is the Fermi velocity, $a = 0.246\,\text{nm}$ is the intralayer lattice constant, and $-t_0$ is the intralayer hopping, where $t_0 = 2.8\,\text{eV}$.

For fixed values of $\mathbf{p}$, s, and η, the Hamiltonian H_0 is a semi-infinite SSH model [10] with hopping parameters $f_{\mathbf{p},\eta}$ and γ_0. As a result, there is an exponentially decaying surface mode with energy 0 when $|f_{\mathbf{p},\eta}| < \gamma_0$, or equivalently when $|\mathbf{p}| < p_0 = \gamma_0/(\hbar v_F)$. Additionally, for such momenta, there are no other surface modes, and the bulk modes have a gap around

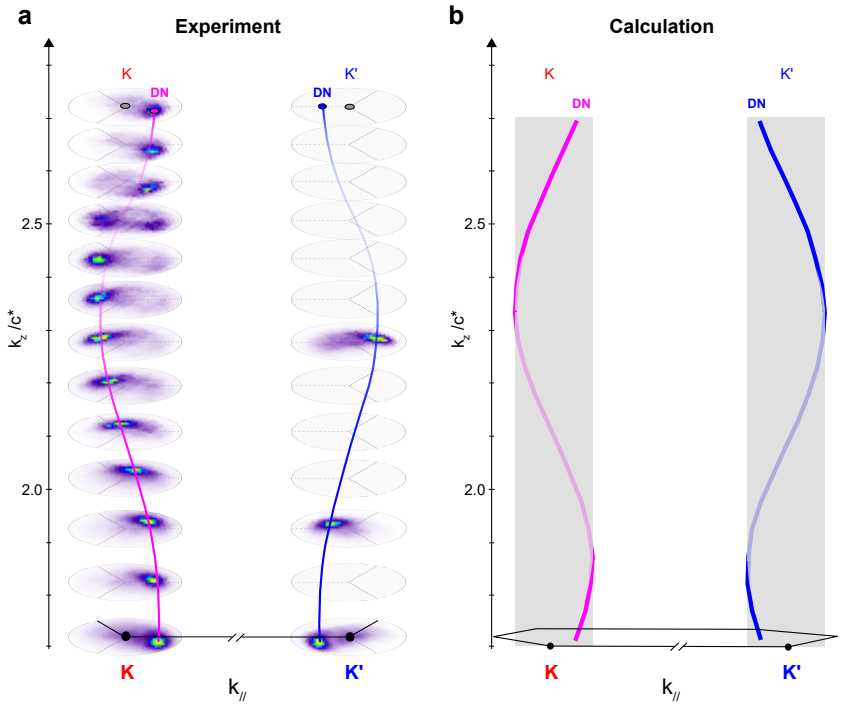

FIG. S8: **Comparison between the experimental and calculated helical Dirac nodal lines at K and K′. a**, Energy contours at K and K′ points measured at 100 meV with photon energies from 40 eV (bottom panel) to 100 eV (top panel), which correspond to $k_z = 1.72c^*$ and $2.72c^*$. **b**, Calculated Dirac nodal lines at K and K′ points from $k_z = 1.70c^*$ to $k_z = 2.70c^*$.

energy 0. The surface mode has creation operator

$$\psi^\dagger_{\mathbf{p},s,\eta} = \sqrt{1-|\mathbf{p}/p_0|^2}\sum_{l=0}^{\infty}(-f_{\mathbf{p},\eta}/\gamma_0)^l c^\dagger_{\mathbf{p},s,\eta,l,A} \tag{4}$$

which is polarized on the A sublattice.

We now consider a screened Coulomb interaction. For electrons in layers l' and l separated by a vector $\mathbf{r}$ in the xy plane, the interaction takes the form

$$V_{l',l}(\mathbf{r}) = \frac{q_e^2}{4\pi\epsilon_0}\frac{e^{-q_0|\mathbf{r}+(l'-l)c\hat{\mathbf{z}}|}}{|\mathbf{r}+(l'-l)c\hat{\mathbf{z}}|} \tag{5}$$

where $c = 0.334\,\mathrm{nm}$ is the interlayer lattice constant, q_e is the electron charge, ϵ_0 is the vacuum permittivity, and $q_0 = 0.01\,\mathrm{nm}^{-1}$ determines the screening strength. The many-body Hamiltonian is formed by projecting this interaction into the surface modes in Eq. (4) and using the "average" or "infinite-temperature" subtraction scheme [11]. This Hamiltonian commutes with the anti-unitary particle-hole symmetry $P\psi^\dagger_{\mathbf{p},s,\eta}P^{-1} = \psi_{-\mathbf{p},-s,-\eta}$.

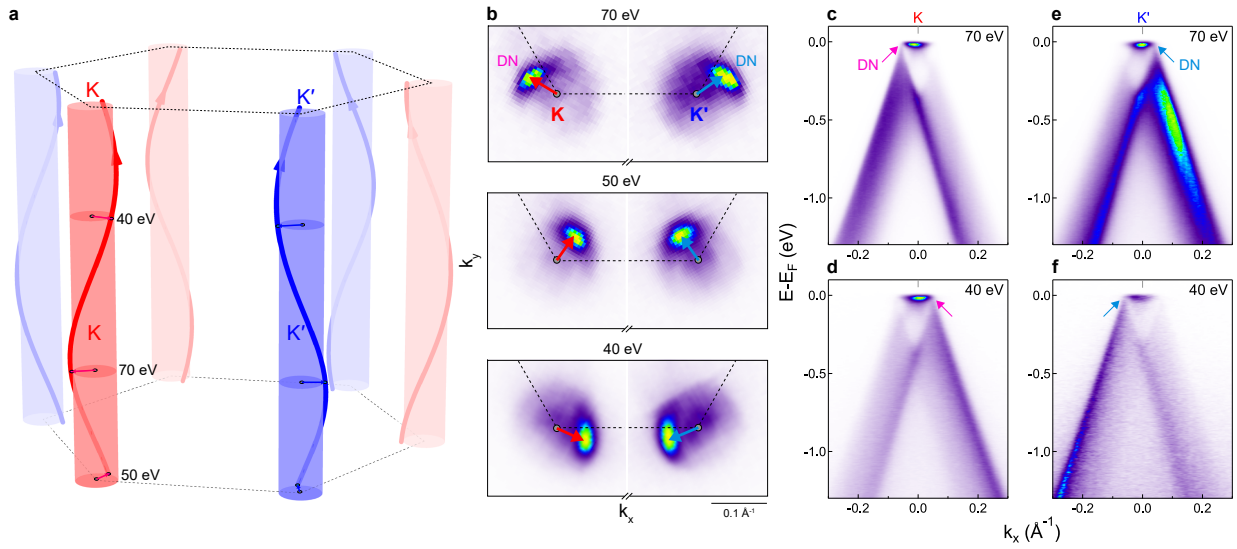

FIG. S9: **Opposite chiralities for helical DNLs at K and K′.** **a**, Schematic illustration to show the opposite helical DNLs near K and K′. Enhanced red and blue shaded ovals indicate the corresponding k_z values with probing photon energies of 40, 50, and 70 eV, which correspond to k_z = -0.27c^*, -0.07c^* and 0.28c^* in the reduced BZ, respectively. **b**, Intensity maps at −100 meV measured at photon energies of 40, 50, and 70 eV to reveal the opposite chiralities for DNLs between K and K′ valleys. Note that the measurements in each valley were performed by rotating the azimuthal angle of the sample to ensure exactly the same experimental geometry, and therefore the observed symmetry reflects the intrinsic symmetry of the sample. The ARPES data are measured on sample S2. **c-f**, Dispersion images measured at photon energies of 70 eV (**c, e**) and 40 eV (**d, f**) by cutting through the Dirac nodes near the K point (**c, d**) and K′ point (**e, f**).

To calculate the doping evolution, we define the filling factor of the top surface topological flat bands (TFBs) only. Note that here the TFBs do not cover the whole BZ, but rather the drumhead TFBs are confined within a momentum boundary being the surface projection of the bulk Dirac nodal line (the circle with momentum diameter of $2p_0 = 2\gamma_0/(\hbar v_F)$ centered at the K or K′ point). Since there are four TFBs corresponding to the two spins and two valleys, the filling factor ν = -2, -1, 0, 1, 2 indicates that 0,1,2,3, or 4 TFBs are filled, respectively, with $\nu = 0$ defined as the particle-hole symmetric point of the top layer. Since the Hartree-Fock calculations include only the TFB states, the surface flat band filling ν we defined is the relevant quantity in this context. From the size of the flat band, the electron density corresponding to full filling of 4 TFBs is $4\pi p_0^2/(2\pi)^2 \approx 8 \times 10^{12}\text{cm}^{-2}$. For Fig. 5

and Fig. S10, we ran self-consistent Hartree-Fock calculations for various filling factors ν, where $\nu = -2$ means the fully empty state and $\nu = 2$ means the fully occupied state. We assumed that continuous translation and rotation symmetries were preserved and used 900^2 unit cells per graphene layer. In order to consider arbitrary fractional fillings, we used grand canonical Hartree-Fock with a temperature of $1\,\mathrm{neV}/k_B$ and converged on the free energy to an absolute tolerance of $1\,\mu\mathrm{eV}$.

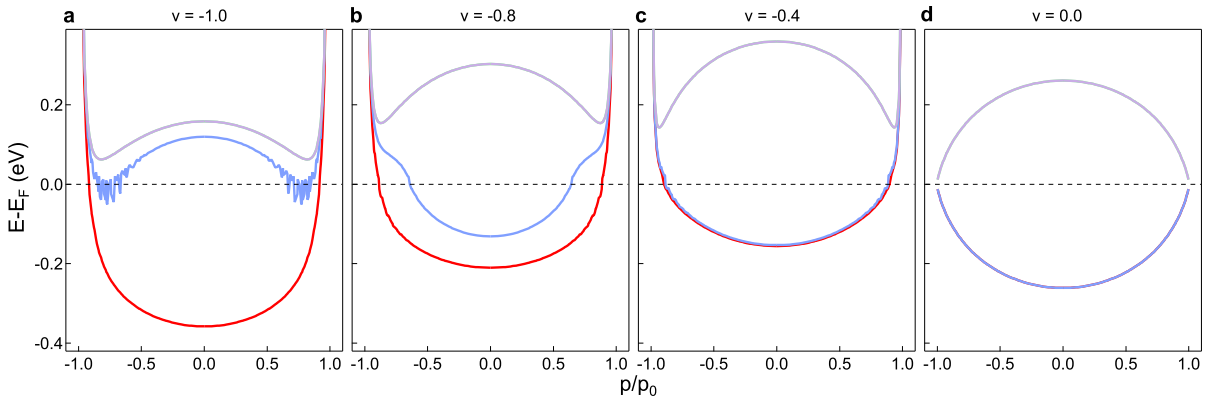

FIG. S10: **Additional Hartree-Fock band structures. a-d**, Self-consistent Hartree-Fock calculations of the TFBs at fillings of $\nu = -1.0$, -0.8, -0.4, and 0.0, respectively. Each panel shows the four resulting Hartree-Fock bands. The top two bands are degenerate. As the filling increases, the second lowest band (blue curve) is filled and eventually becomes degenerate with the lowest band (red curve). The Hamiltonian has exact particle-hole symmetry, so the Hartree-Fock band structure at filling ν is the same as that at filling $-\nu$ if the y axis is negated. See Fig. 5 for similar plots at fillings of $\nu = -1.95$, -1.85, -1.50, and -1.15.

[1] J. McClure, Carbon **7**, 425 (1969).

[2] M. Dresselhaus and G. Dresselhaus, Adv. Phys. **30**, 139 (1981).

[3] M. Koshino and E. McCann, Phys. Rev. B **80**, 165409 (2009).

[4] S. Slizovskiy, E. McCann, M. Koshino, and V. I. Fal'ko, Commun. Phys. **2**, 164 (2019).

[5] G. Chen, A. L. Sharpe, P. Gallagher, I. T. Rosen, E. J. Fox, L. Jiang, B. Lyu, H. Li, K. Watanabe, T. Taniguchi, et al., Nature **572**, 215 (2019).

[6] Y. Liu, N. Zou, S. Zhao, X. Chen, Y. Xu, and W. Duan, Nano Lett. **22**, 2120 (2022).

[7] Y. Shi, S. Xu, Y. Yang, S. Slizovskiy, S. V. Morozov, S.-K. Son, S. Ozdemir, C. Mullan, J. Barrier, J. Yin, et al., Nature **584**, 210 (2020).

[8] C.-H. Ho, C.-P. Chang, and M.-F. Lin, Phys. Rev. B **93**, 075437 (2016).

[9] S. Y. Zhou, G.-H. Gweon, J. Graf, A. V. Fedorov, C. D. Spataru, R. D. Diehl, Y. Kopelevich, AU, D.-H. Lee, S. G. Louie, et al., Nat. Phys. **2**, 595 (2006).

[10] W. P. Su, J. R. Schrieffer, and A. J. Heeger, Phys. Rev. Lett. **42**, 1698 (1979).

[11] Y. H. Kwan, J. Yu, J. Herzog-Arbeitman, D. K. Efetov, N. Regnault, and B. A. Bernevig, arXiv:2312.11617 (2023).